Article

Entropic Forces Drive Cellular Contact Guidance

Antonetta B. C. Buskermolen,[1,7] Hamsini Suresh,[2] Siamak S. Shishvan,[2,3] Andrea Vigliotti,[2,4] Antonio DeSimone,[2,5,6] Nicholas A. Kurniawan,[1,7] Carlijn V. C. Bouten,[1,7] and Vikram S. Deshpande[2,*]

[1]Department of Biomedical Engineering, Eindhoven University of Technology, Eindhoven, North Brabant, Netherlands; [2]Department of Engineering, University of Cambridge, Cambridge, United Kingdom; [3]Department of Structural Engineering, University of Tabriz, Tabriz, East Azarbayjan, Iran; [4]Innovative Materials, Italian Aerospace Research Center, Capua, Caserta, Italy; [5]The BioRobotics Institute, Scuola Superiore Sant'Anna, Pontedera, Pisa, Italy; [6]SISSA – International School for Advanced Studies, Trieste, Italy; and [7]Institute for Complex Molecular Systems (ICMS), Eindhoven University of Technology, Eindhoven, The Netherlands

ABSTRACT Contact guidance—the widely known phenomenon of cell alignment induced by anisotropic environmental features—is an essential step in the organization of adherent cells, but the mechanisms by which cells achieve this orientational ordering remain unclear. Here, we seeded myofibroblasts on substrates micropatterned with stripes of fibronectin and observed that contact guidance emerges at stripe widths much greater than the cell size. To understand the origins of this surprising observation, we combined morphometric analysis of cells and their subcellular components with a, to our knowledge, novel statistical framework for modeling nonthermal fluctuations of living cells. This modeling framework is shown to predict not only the trends but also the statistical variability of a wide range of biological observables, including cell (and nucleus) shapes, sizes, and orientations, as well as stress-fiber arrangements within the cells with remarkable fidelity with a single set of cell parameters. By comparing observations and theory, we identified two regimes of contact guidance: 1) guidance on stripe widths smaller than the cell size ($w \leq 160 \ \mu m$), which is accompanied by biochemical changes within the cells, including increasing stress-fiber polarization and cell elongation; and 2) entropic guidance on larger stripe widths, which is governed by fluctuations in the cell morphology. Overall, our findings suggest an entropy-mediated mechanism for contact guidance associated with the tendency of cells to maximize their morphological entropy through shape fluctuations.

INTRODUCTION

Cellular organization plays a crucial role in the microarchitecture of tissues and dictates their biological and mechanical functioning (1–3). This organization is often the result of the response of cells to the anisotropy of their microenvironment, which induces cells to migrate preferentially along the direction of anisotropy (4,5)—a phenomenon called contact guidance (6–8). Here, we make a distinction between directed cell migration that results from contact guidance (4,5) and the more fundamental contact guidance effect itself, which refers to cell alignment in response to environmental anisotropy (9–11). Indeed, contact guidance is known to affect various downstream cell behaviors, including survival, motility, and differentiation (11,12). Uncovering the origins of cellular contact guidance is therefore critical not only for understanding tissue morphogenesis and regeneration but also for predicting disease progression such as cancer invasion (13,14).

Despite the importance of cellular organization in all facets of tissue biology, the fundamental question of how a cell organizes itself in physiological tissue context is still poorly understood (15,16). Almost exclusively, the rationalization of contact guidance has been based on the different components of the mechanotransduction pathway. Some of the more common theories hypothesize that 1) mechanical restriction imposed by the substrate geometry drives the polarization of linear bundles of F-actin (8), 2) the tendency of cells to maximize their focal adhesion areas drives their alignment along ridges on grooved substrates (17), and 3) sharp discontinuities in the substrates (e.g., edges of microgrooves) induce cell alignment by triggering actin polymerization and thereby focal adhesion formation at these locations (18). However, these explanations do not provide a general framework for understanding contact guidance (i.e., cannot be extended beyond the particular experimental setup for which they were proposed). A systematic and integrated framework for contact guidance as observed in response to a host of biophysical (microgrooves, substrate elasticity) and/or biochemical (adhesive patterns, ligand density) cues has, to date, proved elusive.

The aim of this investigation is to elucidate the general biophysical mechanisms underlying contact guidance of individual cells. Various in vitro chemical micropatterning approaches have been developed to study cellular contact guidance as model systems to simplify the highly complex in vivo environments (19,20). We followed such an approach and seeded a low density of myofibroblasts (specifically, human vena saphena cells; see Materials and Methods) on effectively rigid substrates microprinted with FN stripes of widths w, ranging from greater than 1.5 mm (resembling a homogeneous two-dimensional (2D) substrate) to 50 μm; see Fig. 1 a. This enabled us to investigate contact guidance as affected by extra cellular matrix proteins in the absence of short-range cell-cell interactions (21) and long-range interactions via substrate elasticity (22). Surprisingly, we observed that even in this highly simplified model system, contact guidance commences at stripe widths much greater than the average cell size. None of the theories mentioned above to rationalize contact guidance, which are based on the interaction of the cell with the edges of the geometrical features used to guide them, can provide an explanation for this observation.

To interpret our unanticipated experimental observations, we combined detailed morphometric analysis of cells (and their subcellular components) with a, to our knowledge, novel statistical framework that models the nonthermal fluctuations of living cells. These fluctuations, fueled by the exchange of nutrients between the cell and the surrounding nutrient bath, allow the cell to explore a large number of morphological microstates. However, these fluctuations are constrained by the fact that the cell maintains a homeostatic state and by environmental cues such as, in our case, adherence to FN stripes. In our approach, we assume that the distribution of observed microstates is the one that satisfies these constraints and contains the overwhelming number of morphological microstates (i.e., the distribution that maximizes the morphological entropy). Then, the statistics of biological observables such as cell shape and orientations and spatial distributions of cytoskeletal proteins is derived from that maximal entropy distribution of morphological states of the cell.

The outcome of our analysis is that, when cells are confined to stripes of finite width, the maximal entropy orientation distribution of cells is not the uniform, but rather one that is peaked around the orientation of the stripe. More specifically, our statistical framework leads to the prediction that there exists a transition stripe width w_{crit}, above which contact guidance on the stripes is entirely governed by entropic fluctuations of the cell morphology. At stripe widths smaller than w_{crit}, the confining action of FN stripes causes biochemical changes within the cell that lead to the enhanced polarization of stress fibers and an increase in contact guidance. In fact, our statistical approach delivers a quantitative measure of the strength of contact guidance through a computable thermodynamic guidance force. This guidance force increases with decreasing w and can be used to identify two distinct regimes of contact guidance, one purely entropic and one that is biochemically mediated.

A key outcome of this work is that the ordering of cell orientation—a signature of contact guidance—emerges as a consequence of morphological fluctuations of the cell that actually maximize the morphological entropy (or disorder) of cells. Although our results are specific to the phenomenon of contact guidance, our methods are general, and they suggest the possibility of a general statistical active-matter theory for the response of living cells to environmental cues, based on maximization of morphological entropy subject to the constraint of homeostasis.

MATERIALS AND METHODS

Microcontact printing was used to pattern single (FN) adhesive stripes of width w, ranging from 50 to 1570 μm, spaced 500 μm apart using previously established protocols (23). Briefly, the stripe patterns were generated on a silicon master by deep reactive-ion etching (Philips Innovation Services, Eindhoven, the Netherlands) from a chromium photomask (Toppan Photomask, Corbeil Essonnes, France). The silicon surface was passivated with fluorosilane, and microstamps were obtained by molding the silanized silicon master with polydimethylsiloxane (PDMS, Sylgard 184; Dow Corning, Midland, MI) and a curing agent (10:1) and permitted to cure overnight at 65°C. The cured PDMS stamp containing the desired features was then peeled off from the master, cleaned by sonicating it in 70% ethanol for 30 min, and dried using compressed air. The structured surface of the PDMS stamps was inked for 1 h at room temperature with a 50 mg mL^{-1} rhodamine fibronectin (FN) solution (Cytoskeleton, Denver, CO). Flat PDMS-coated glass coverslips served as the substrates on which microprinting was conducted. These substrates were first oxidized in an ultraviolet-ozone cleaner (PDMS ultraviolet-ozone cleaner; Novascan, Ames, IA) for 8 min, and then the FN-coated stamps (first dried under compressed air) were gently deposited on the substrates for 15 min at room temperature. Uncoated regions of the substrates were blocked by immersing the micropatterned coverslips for 5 min in a 1% solution of Pluronic F-127 (Sigma-Aldrich, St. Louis, MO). Finally, the coverslips were washed thrice with phosphate-buffered saline (PBS) and stored in PBS at 4°C until use. A PDMS stamp without any features was used to print a homogeneous pattern of FN on a flat PDMS surface, which was used as the control substrate.

Cell culture

Human vena saphena cells were harvested from the vena saphena magna obtained from patients according to Dutch guidelines of secondary use material and have previously been characterized as myofibroblasts (24). The myofibroblasts were cultured in advanced Dulbecco's modified Eagle's medium (Invitrogen, Breda, the Netherlands) supplemented with 10% fetal bovine serum (Greiner Bio-One, Monroe, NC), 1% penicillin/streptomycin (Lonza, Basel, Switzerland), and 1% GlutaMax (Invitrogen). Only cells with a passage lower than 7 were used in this study. To avoid cell-cell contact between the cells, the micropatterned substrates were seeded with a cell density of 500 cells cm^{-2} and cultured for 24 h at 37°C in 5% CO_2.

Cell fixation and staining

For visualization of the focal adhesions, actin cytoskeleton, and the nucleus, the myofibroblasts were fixed with 4% formaldehyde in PBS (Sigma-Aldrich) 24 h after cell seeding. The cells were then permeabilized with 0.5% Triton-X-100 (Merck, Kenilworth, NJ) for 15 min, blocked for 30 min with 4% goat serum in PBS, and incubated with the primary anti-vinculin
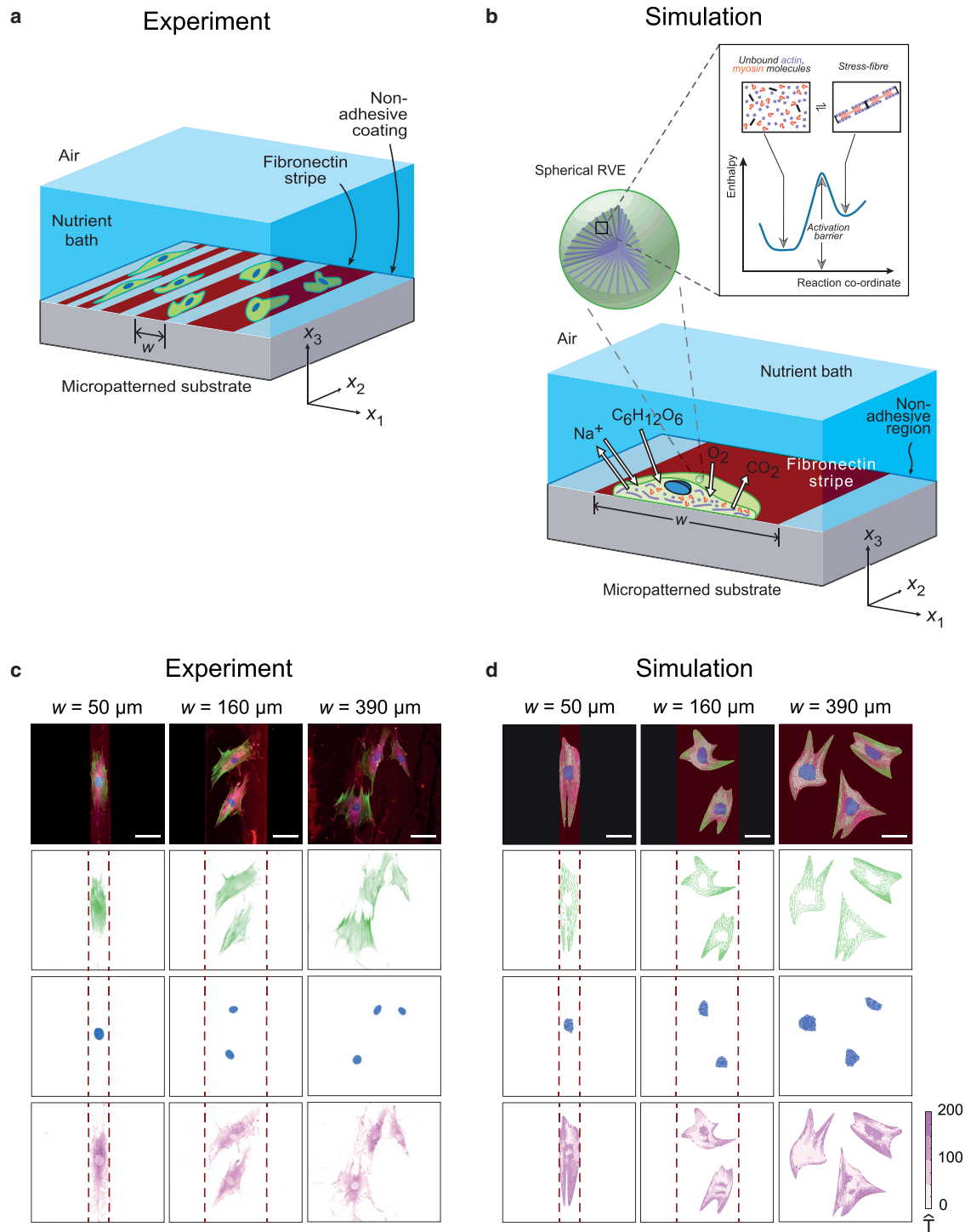
FIGURE 1 Experimental setup and representative images of the experimental data and simulations. (*a*) A sketch of the experimental setup of myofibroblasts seeded on a flat substrate micropatterned with FN (*maroon*) stripes of width *w* is shown. (Although each experimental substrate had one stripe width, for conciseness, the sketch shows different stripe widths on the same substrate.) (*b*) An illustration of the cell model employed in the simulations using homeostatic mechanics framework is given. The sketch shows a section of a cell on a FN stripe of width *w* and exchanging species with the nutrient bath. The inset shows a representative volume element of the cell cytoplasm containing polymerized actomyosin stress fibers and the unbound proteins, along with the energy landscape that governs the equilibrium of these proteins. (*c*) Immunofluorescence images of myofibroblasts on FN stripes of 50, 160, and 390 μm showing the actin cytoskeleton (*green*), nucleus (*blue*), and focal adhesions (*magenta*) are given; the edges of the stripes are indicated by dashed lines. (*d*) Corresponding predictions from the homeostatic mechanics framework with focal adhesions parametrized by the magnitude of the normalized traction $\widehat{T}$ are shown (see Supporting Materials and Methods, Section S2.5.1). The scale bar in (*c*) and (*d*) represents 60 μm, and the width of the FN stripes is indicated by the maroon dashed lines for the two narrowest stripes. To see this figure in color, go online.

antibody IgG1 (V9131; Sigma-Aldrich). Subsequently, samples were incubated with the secondary antibody goat anti mouse-Alexa Fluor 647 (Molecular Probes, Eugene, OR) 1:500 and fluorescein isothiocyanate-conjugated phalloidin (15500, Phalloidin-Atto 488; Sigma-Aldrich) 1:200 for staining the actin cytoskeleton. Finally, the samples were incubated with 4′,6-diamidino-2-phenylindole (Sigma-Aldrich) for 5 min for immunofluorescence of the nucleus and mounted onto glass slides using Mowiol (Sigma-Aldrich). The images of the cells were acquired using an inverted microscope (Zeiss Axiovert 200M; Zeiss, Gottingen, Germany).

Image analysis

Fluorescent microscopy images were recorded at 20 and 40× magnification and then analyzed using a custom-built Mathematica (Mathematica, Version 11.1; Wolfram Research,) script as described previously (24). The binarized images of the profile of each cell and nucleus were fitted with an ellipse using a least-square algorithm (24) and used to quantify observables that include 1) orientation ϕ that measures the angle between the major axis of the best-fit ellipse and the stripe direction x_2 (Fig. 2 b); 2) the aspect ratio A_s, defined by the ratio of the lengths of the major axis/minor axis of the best-fit ellipse; and 3) the order parameter Θ, defined as (21)

$$\Theta \equiv \sqrt{\langle \cos 2\phi \rangle^2 + \langle \sin 2\phi \rangle^2}, \tag{1}$$

where $\langle \cdot \rangle$ denotes the ensemble average over all measurements. The cell and nucleus area were directly determined from the area enclosed within the respective profiles; readers are referred to (24) for more details on the analysis of the data. For each stripe width, three independent experiments were performed, and at least 50 cells were analyzed per stripe width.
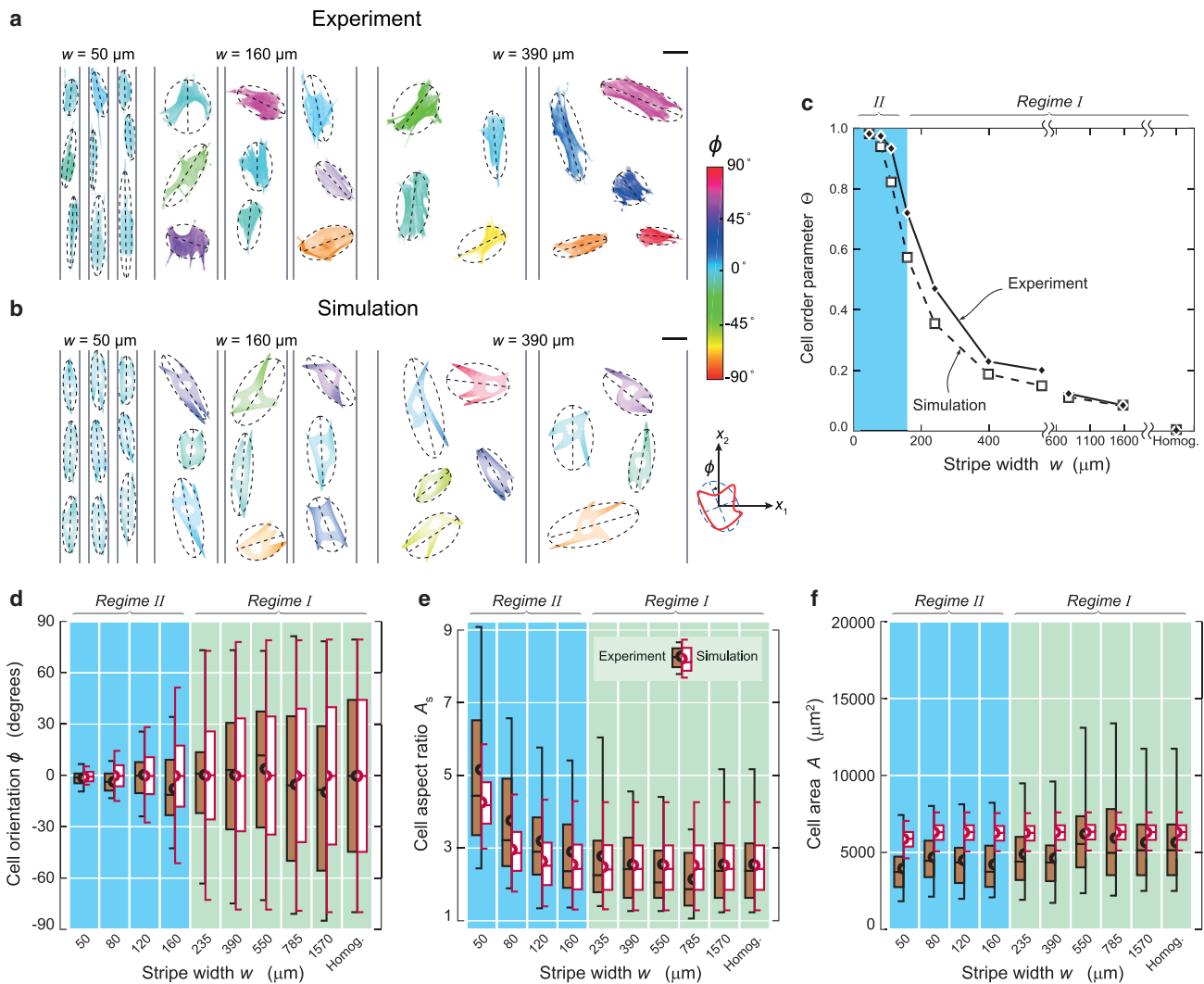
FIGURE 2 Experimental and computational data on key observables. Images of randomly selected (a) experimentally observed and (b) computationally predicted cell morphologies, showing their actin cytoskeleton and shaded to indicate the cell orientation ϕ, are given (definition of ϕ shown in the *inset*, with the best-fit ellipses and the corresponding major axis indicated on the cell images). The images are shown for cells on three selected widths of FN stripes with the scale bar in (a) and (b) representing 60 μm. (c) Measurements and predictions of the cell orientational order parameter Θ vs. stripe width w are shown. Box-and-whisker diagrams of experimental and computational data of the distributions of (d) cell orientation ϕ, (e) aspect ratio A_s, and (f) area A for the range of stripe widths investigated here are given. The boxes show the quartiles of the distributions, with the whiskers indicating the outliers in the experiments and the 5th and 95th percentiles of the distributions in the simulations. The mean of the distributions is depicted by semicircles for both measurements and simulations. In (c)–(f), the two regimes of contact guidance transitioning at a stripe width $w \approx 160$ μm are indicated, and the experimental data set comprised at least 50 observations per stripe width. To see this figure in color, go online.

Box-and-whisker diagrams (showing the quartiles, means, and outliers) of cell and nuclear area, aspect ratio, and orientation were constructed from the data for these 50 cells on each stripe width. The spatial distributions of the stress-fiber orientations $\overline{\varphi}$ and the associated cytoskeletal order parameter $\mathcal{R}$ were extracted from the actin-stained immunofluorescence images, as described in detail in Supporting Materials and Methods, Section S1.

RESULTS

Cell alignment increases with decreasing stripe width

To investigate the origins of cellular contact guidance, we seeded myofibroblasts on micropatterned FN stripes of width w, ranging from 50 μm to homogeneous substrates with $w \rightarrow \infty$. Outside the stripes, cell adhesion is prevented by treatment with a 1% solution of Pluronic F-127 (see Materials and Methods). A schematic illustration of our experimental setup is shown in Fig. 1 a, in which the FN stripes are represented in maroon and the cells in green. The cells were fixed and stained for actin, vinculin, and the nucleus 24 h after seeding. Representative immunofluorescence images (from at least 50 observations over three independent experiments) of the actin cytoskeleton (*green*), nucleus (*blue*), and focal adhesions (vinculin in *magenta*) of cells on FN (*maroon*) stripes of width $w = 50$, 160, and 390 μm are shown in Fig. 1 c (see Fig. S1 a for representative observations on all stripe widths investigated here). These images suggest that although the orientation of the actin cytoskeleton and nucleus are reasonably coordinated to the cell shape, the focal adhesions are spread nearly evenly throughout the cells. A picture that consistently emerges from these images is that cells align more on the narrower FN stripes than on wider stripes, demonstrating the emergence of contact guidance due to the FN micropatterns.

To further illustrate the effect of substrate micropatterns on cell morphology, randomly selected images of cells are included in Fig. 2 a, with the actin stress fibers shaded in a color to represent the cell orientation ϕ of the particular configuration. The cell orientation ϕ is defined as the angle between the major axis of the best-fit ellipse to the cell shape and the stripe direction x_2; see Materials and Methods. Nearly all cells on the $w = 50$ μm stripes are aligned with the stripes ($\phi \approx 0°$), whereas there is a much larger spread of cell orientations for cells on wider stripes. Although these images give a flavor of the observations, they do not capture the diversity of the observations, which is best quantified via statistical indicators. The extent of cell alignment to extracellular cues is usually quantified by the cell orientational order parameter Θ (Materials and Methods), where $\Theta = 0$ corresponds to a completely random distribution of ϕ and $\Theta = 1$ when all cells have identical orientations (21). In our experiments, cell alignment steadily increases with decreasing w, reaching $\Theta \approx 1$ for $w \leq 160$ μm, suggesting complete alignment of the cells with the stripes in this regime (Fig. 2 c). Surprisingly, $\Theta \approx 0$ only occurs in the homogeneous substrate limit ($w \rightarrow \infty$), whereas cells align with the stripes for all $w \leq 1570$ μm that we investigated, even though cell sizes (as parametrized by the length of the major axis of the best-fit ellipse) are typically on the order of 130 μm.

In line with the trend for Θ, the spread in ϕ decreases with decreasing w over the entire range of stripe widths investigated here, as shown in the box-and-whisker plots (Fig. 2 d). To understand the underlying reason for this spread in cell orientation, we also quantified the effect of the FN stripe width on cell morphology and size. To represent the shape of the cells, we determined the cell aspect ratio A_s (defined as the ratio between the major axis/minor axis of its best-fit ellipse) and cell area A (see Materials and Methods). Intriguingly, the dependence of the spread of ϕ on w is not reflected in these observables, with the distribution of A being independent of w, whereas the mean A_s only begins to increase for $w \leq 160$ μm (i.e., in the regime where $\Theta \approx 1$); see Fig. 2, d–f. These findings underline the need to better understand the origins of the contact guidance response, particularly in a statistical context.

Homeostatic mechanics predictions reproduce morphometric observations

The experimental system investigated here consists of cells responding to extracellular cues (i.e., adhesive FN stripes) through intracellular processes, including cytoskeletal dynamics. The response of this complex system is recorded through a range of observables, all of which exhibit large variations (Fig. 2, d–f) but with trends clearly emerging when the statistics of these observables are analyzed. This motivates our choice of a statistical modeling framework, which we call homeostatic mechanics, in which, just as in the experimental system, observables fluctuate, whereas trends (and understanding) emerge once these observables are viewed statistically (Supporting Materials and Methods, Section S2). This framework has previously been shown to successfully capture a range of observations for smooth muscle cells seeded on elastic substrates (25), giving us confidence to investigate its generality in terms of predicting the contact guidance behavior of the myofibroblasts reported here.

The homeostatic mechanics framework recognizes that the cell is an open system that exchanges nutrients with the surrounding nutrient bath (Fig. 1 b). These high-energy nutrient exchanges fuel large fluctuations (much larger than thermal fluctuations) in cell response associated with various intracellular biochemical processes. However, these biochemical processes attempt to maintain the cell in a homeostatic state, i.e., the cell actively maintains itself out of thermodynamic equilibrium (26) by maintaining its various molecular species at a specific average number over these fluctuations that is independent of the environment (27). More specifically, homeostasis is the ability of

a living cell to maintain, via coupled and interconnected biomechanical processes, the concentration of all internal species at a fixed average value independent of the environment over all its nonthermal fluctuations (at least over the interphase period of the cell cycle and in the absence of any imposed shock such as starving the cell of nutrients). This implies that over the fluctuations of the cell from a fixed reference state (e.g., cell in suspension), $\langle \Delta N_i \rangle = 0$, where ΔN_i is the change in the number of molecules of species i from its reference value and $\langle x \rangle$ is the average of x over the ensemble of states sampled over the nonthermal fluctuations. These fluctuations alter the cell morphology, and each morphological microstate has a unique equilibrium Gibbs free energy $G = \sum_i \mu_i N_i$, where μ_i is the chemical potential of species i. Using the Gibbs-Duhem relation, we then rewrite this in terms of the reference state as $G = G_0 + \sum_i \mu_i^0 \Delta N_i$, where μ_i^0 is now the chemical potential of species i in the reference state. Upon employing the homeostatic constraint that $\langle \Delta N_i \rangle = 0$, we have $\langle G \rangle = G_0$, i.e., irrespective of the environment, the ensemble average Gibbs free energy is equal to that of the cell in suspension. This is a universal constraint that quantifies the fact that living cells maintain themselves away from thermodynamic equilibrium but yet attain a stationary state. Then, recognizing that biochemical processes such as actin polymerization and treadmilling provide the mechanisms to explore morphological microstates, we employ the ansatz that the observed distribution is the one with the overwhelming number of microstates, i.e., the distribution that maximizes the morphological entropy subject to the constraint that $\langle G \rangle = G_0$ and that all microstates are adhered within the FN stripes.

The implementation of the homeostatic mechanics approach described above requires a specific model for the mechanobiochemistry of stress fibers and focal adhesions (28–30). Here, we employ a relatively simple model, wherein the cell consists of a passive elastic nucleus within a cytoplasm that is modeled as comprising an active stress-fiber cytoskeleton in which the actin and myosin proteins exist either in unbound or in polymerization states (Fig. 1 b) and elements such as the cell membrane, intermediate filaments, and microtubules are all lumped into a single passive elastic contribution; see Supporting Materials and Methods, Section S2 for details, including the cell parameters used to characterize the myofibroblasts with the simulation code posted at (31).

Fig. 1 d shows representative images of computed cell morphologies and the corresponding actin, nucleus and focal adhesion organizations (for $w = 50$, 160, and 390 μm; directly comparable to observations in Fig. 1 c). These morphologies have been selected from the computed ensemble of all morphological microstates the cell samples (i.e., the homeostatic ensemble) with the constraint that the morphologies have a cell aspect ratio equal to the mode of the distri-

bution for the particular stripe width (see Supporting Materials and Methods, Section S2.5 for the precise definitions of quantities plotted in Figs. 1 d and S1 b for corresponding predictions on all stripe widths investigated here). Overall, the cell morphologies are similar to the experimental observations, with the stress fibers aligning with the cell orientation and the focal adhesions being distributed throughout the cell. Moreover, consistent with the experiments, the cells are randomly oriented on the wider FN stripes but nearly aligned with $\phi \approx 0°$ on the $w = 50$ μm stripes (Fig. 2 b). To make this comparison more quantitative, we also determine the order parameter Θ from the entire computed homeostatic distribution of cell morphologies and find excellent agreement with the experimental data over the entire range of w (Fig. 2 c). Furthermore, the homeostatic mechanics framework accurately reproduces not only the averages but also the distributions of the observed cell orientation ϕ as quantified in terms of the box-and-whisker diagrams (Fig. 2 d). The predictive capability also extended to the cell aspect ratio (Fig. 2 e), although now the model underpredicts the spread for the small stripe widths. However, in general, the observed spread in the cell areas is larger than model predictions (Fig. 2 f). We attribute these discrepancies to the fact that the model assumes a 2D cell (for computational efficiency), and this restricts the spreading of the cell compared to the three-dimensional cell in the experiments (32). Corresponding morphometric observations and predictions for the nucleus are presented in Fig. S2.

Emergence of two regimes of contact guidance: Wide versus narrow stripes

Both experimental data and model predictions suggest a transition value $w_{crit} \approx 160$ μm that divides the cell response into two regimes: regime I for $w > w_{crit}$, in which cell alignment occurs in the absence of significant changes of cell shape, and regime II for $w \leq w_{crit}$, in which cell alignment is accompanied by shape changes (Fig. 2, d–f). This transition stripe width is also consistent with the experiments and predictions that cell alignment (as well as nuclear alignment; see Fig. S2) is low for $w \gg w_{crit}$ with almost complete alignment ($\Theta \approx 1$) at widths $w \leq 160$ μm. Intrigued by this observation, we interrogated the homeostatic mechanics model to evaluate the dependence of total Gibbs free energy, the cytoskeletal free energy, and the elastic energy of the cell on stripe width (Fig. S3) because these quantities are typically not directly measurable in experiments. The predictions show that the distributions of cellular energies are invariant to stripe width for $w > w_{crit}$ and thus hint at the existence of two distinct mechanisms of contact guidance or cell alignment:

1) A regime I for $w > w_{crit}$ in which cell alignment is accomplished by reorientation of the cell at fixed area

and aspect ratio, with no associated changes in cellular energies. This suggests that alignment in this regime is not driven energetically but rather by entropic forces (made explicit subsequently) associated with morphological fluctuations of the cell.

2) A regime II for $w \leq w_{crit}$ in which cell alignment is accompanied by changes in the cell energies and shapes and hence thought to be mediated by biochemical changes within the cells.

Regime I: Entropic alignment of cells for stripe widths larger than the cell size

Cells on substrates with $w > 160$ μm have a mean area and aspect ratio $\overline{A} \approx 5000$ μm^2 and $\overline{A}_s \approx 2.6$, respectively (Fig. 2 d). Approximating the shape of the cell to be an ellipse, the semimajor axis ℓ_e follows $\ell_e = \sqrt{(\overline{A}_s \overline{A})/\pi}$. Thus, cells located at the center of FN stripes of $w > 2\ell_e \approx 130$ μm are expected to assume all orientations ϕ with equal probability, but the orientation of cells on smaller w is expected to be restricted by the finite widths of the FN stripes. The critical stripe width of $w_{crit} = 160$ μm is remarkably consistent with $2\ell_e$. Here, we shall use this simple observation to develop an understanding of the mechanisms that result in cell alignment in regime I.

Predictions of the joint probability density function $p(x_c, \phi)$ of the cell centroid being located at position $x_1 = x_c$ within the stripe and having an orientation ϕ are shown in Fig. 3, a–c for three stripes of widths in the range 50 $\mu m \leq w \leq 390$ μm. For $w = 390$ μm, $p(x_c, \phi)$ is nearly uniform, indicating that cells are equally probable to exist at all locations and orientations within the stripe. With decreasing stripe width, $p(x_c, \phi)$ starts to become more heterogeneous. Specifically, although cells with centroids near the center $x_1 = 0$ of the stripe have equal probability to exist in all orientations, cells near the edges of the stripes are more likely to be aligned with the stripes ($\phi = 0°$). This heterogeneity is clearly seen in Fig. 3 b, in which for $w = 160$ μm, the probability of misaligned cells (defined arbitrarily here as cells with $|\phi| \geq 45°$) is diminished even for cells with $x_c \approx 0$ and so is the probability of finding a cell near the stripe edges. For the smallest stripe width ($w = 50$ μm), the model predicts that cells are restricted to have their centroids at $x_c \approx 0$ and aligned to the stripes. This transition in the probability distribution occurs at $w \approx w_{crit} \approx 2\ell_e$ because the major axis of the cell is now longer than the width w of the FN stripes, and therefore the cells cannot lie orthogonal to the stripes with $|\phi| = 90°$. The model thus suggests that cell alignment in regime I is a direct consequence of the fact that cells near the edges of the stripes necessarily need to be aligned with the stripe directions: with decreasing w, the probability of cells being closer to the stripe edges increases, resulting in an increase in the average alignment as parametrized by the order parameter Θ. We refer to this as an entropic alignment because it is accompanied by no changes
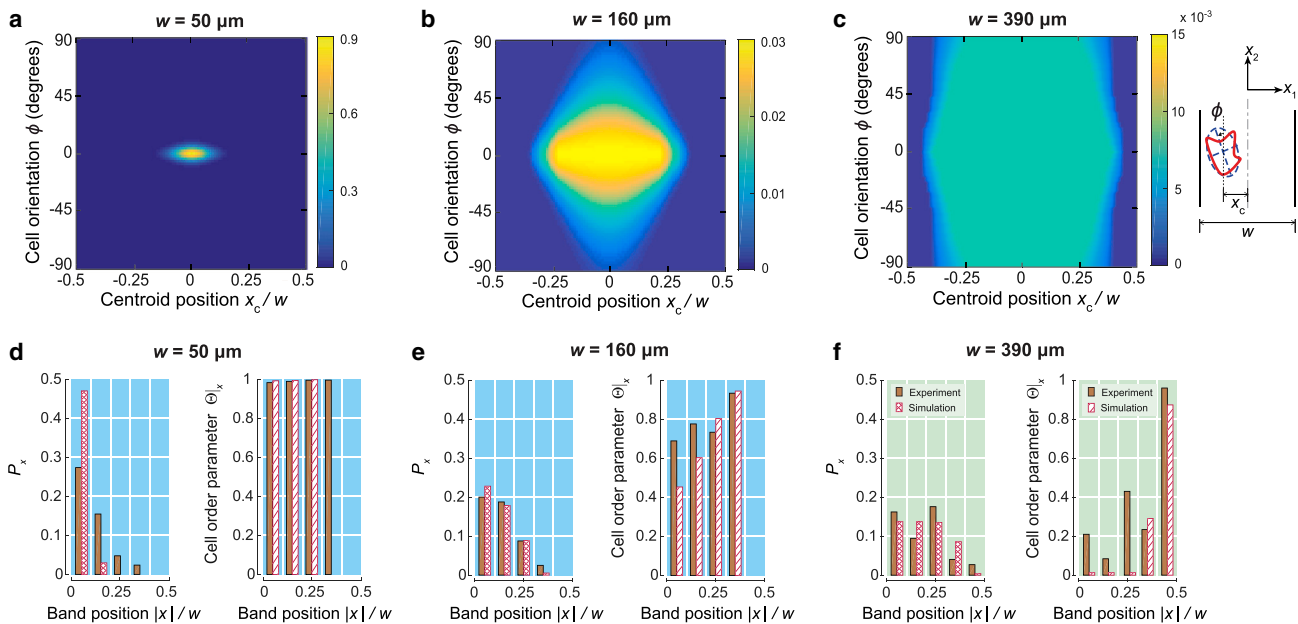

FIGURE 3 (a–c) Predictions of the joint probability density distributions $p(x_c/w, \phi)$ of the cell centroid being located at position $x_1 = x_c$ within the stripe and having an orientation ϕ. Results are shown for three selected stripe widths w, with the inset defining x_c and ϕ. With decreasing w, the distributions become more heterogeneous, with cells unable to adopt an isotropic distribution of orientations, especially near the stripe edges. Note the differences in the color scales of the probability densities between the different subparts. (d–f) Measurements (from 50 observations per stripe width) and predictions of the probability P_x of the cell centroid location across the stripe (left) and the conditional order parameter $\Theta|_x$ of cells within each band centered at location x (right). In plots (d)–(f), each stripe is divided into bands of equal width, and the symmetric results shown for $|x|$, varying from the stripe center ($x = 0$) to the stripe edge at $|x|/w = 0.5$. To see this figure in color, go online.

to the distribution of the free energies the cell attains as it fluctuates over its homeostatic state (Fig. S3). Rather, it is only associated with the spatial restriction that the FN stripes impose on the states (or morphologies) the cell is allowed to attain and is therefore entropic in origin.

A key assumption in the model is that on the experimental timescales (the 24 h the cells were cultured on the micropatterned substrates) over which the orientations and positions of the cells fluctuate, the behavior is "ergodic" (i.e., the cells sample all states compatible with the constraints with equiprobability). The consequence is that the distribution of morphological microstates cells assume maximizes their morphological entropy. Recalling that a morphological microstate corresponds to both the cell morphology as well as its position, a corollary of this assumption is that over these timescales, the cells have no memory such that the cells might align while near the stripe edges, but they lose the memory of that state as they migrate to the interior of the stripes. Based on the entropic ansatz that all allowable states are equally probable, the model predicts that 1) cells near the center of stripes of width $w > 2\ell_e$ are equally likely to exist in any orientation and 2) given that cells near the stripe edges exist in fewer orientations, cells are less likely to be found near the stripe edges. To confirm that the experimental results agree with these predictions, we divide each stripe into bands of breadth $w/10$ and measure 1) the probability P_x of finding a cell in a band with midpoint located at $x_1 = |x|$ and 2) the corresponding order parameter $\Theta|_x$ of cells located within that band. These measurements for cells on stripes of widths $w = 50$, 160, and 390 μm, together with the corresponding model predictions, are included in Fig. 3, d–f. Indeed, in both the measurements and predictions, the probability of finding a cell in a band near the stripe edge, i.e., $|x|/w \approx$ 0.5 is lower than finding the cell at the center of the stripes. By contrast, although the order parameter $\Theta|_x \approx 1$ in all bands for the $w = 50$ μm stripe, the order parameter is higher in bands near the stripe edges compared to bands near the stripe center for the two larger stripe widths. The consistency and agreement between measurements and predictions strongly suggests the validity of the no-memory assumption, with cell alignment (Fig. 2 b) only resulting from those cells that directly interact with the stripe edges.

Regime II: Biochemical changes accompany alignment at small stripe widths

The enhanced cell alignment in regime II ($w \leq 160$ μm) is accompanied by changes to cell shape as parametrized by the cell aspect ratio (Fig. 2 e). We hypothesize that these shape changes go hand-in-hand with biochemical changes within the cells. To test this idea, we measured the dispersion of actin stress-fiber orientations φ within cells and used this distribution as a direct observable indicative of the biochemical state of the cell. Specifically, we monitored local stress-fiber orientations $\varphi(x_i)$ with respect to the x_2

direction at every location x_i within the cell and defined a stress-fiber orientation measure $\overline{\varphi}(x_i)$ that is invariant to rigid-body rotations of the cell (Supporting Materials and Methods, Section S1.2). Fig. 4 a shows representative images of observed cells with the stress fibers colored by their rotationally invariant orientation $\overline{\varphi}$. Cells on $w = 50$ μm stripes have a near-uniform distribution of stress-fiber orientations with $\overline{\varphi} \approx 0^\circ$ throughout the cell; however, there is a larger dispersion in $\overline{\varphi}$ for cells on wider FN stripes. To quantify this observation more precisely, we evaluated probability density functions $p(\overline{\varphi})$ by assembling the measurements of $\overline{\varphi}$ over all imaged cells (at least 50 cells) for each stripe width. The distributions $p(\overline{\varphi})$ shown in Fig. 4 c hardly change in regime I ($w > 160$ μm) but become increasingly peaked with mode at $\overline{\varphi} = 0^\circ$ in regime II ($w \leq 160$ μm).

To succinctly capture this decrease in the dispersion of $\overline{\varphi}$, we introduce a cytoskeletal order parameter $\mathcal{R}$ (analogous to the cell orientation order parameter Θ) as

$$\mathcal{R} \equiv \sqrt{\left(\int_{-\frac{\pi}{2}}^{\frac{\pi}{2}} p(\overline{\varphi}) \cos 2\overline{\varphi} d\overline{\varphi} \right)^2 + \left(\int_{-\frac{\pi}{2}}^{\frac{\pi}{2}} p(\overline{\varphi}) \sin 2\overline{\varphi} d\overline{\varphi} \right)^2}.$$

(2)

We emphasize that $\mathcal{R}$ is a statistic defined over the entire ensemble of observed cells through the distribution $p(\overline{\varphi})$ and differs from definitions used in previous studies (33,34). This definition not only gives more robust results but is also more in line with the fluctuating response of cells as proposed by the homeostatic statistical mechanics framework; see detailed discussion in Supporting Materials and Methods, Sections S2.5.3 and S2.5.4. We find that $\mathcal{R}$, unlike Θ, is approximately constant for stripe widths $w > 160$ μm but rises sharply for $w \leq 160$ μm (Fig. 4 d). This suggests that no changes to the biochemical state of the cells occur in regime I, but cell alignment is accompanied by biochemical changes in regime II. The corresponding predictions of the spatial distributions of stress-fiber orientations $\overline{\varphi}$, the probability density functions $p(\overline{\varphi})$, and $\mathcal{R}$ are all in remarkable correspondence with detailed experimental measurements of the state of the cells; see Fig. 4, b–d, respectively, and Supporting Materials and Methods, Section S2.5.3 for details of the calculation of $\overline{\varphi}$ from the model. In particular, both experimental observations and model predictions show negligible enhancement in stress-fiber alignment in regime I but increasing stress-fiber polarization with decreasing stripe width in regime II.

Thermodynamic forces help delineate the two regimes of alignment

Given the high level of agreement between the detailed experimental data and the predictions of the homeostatic
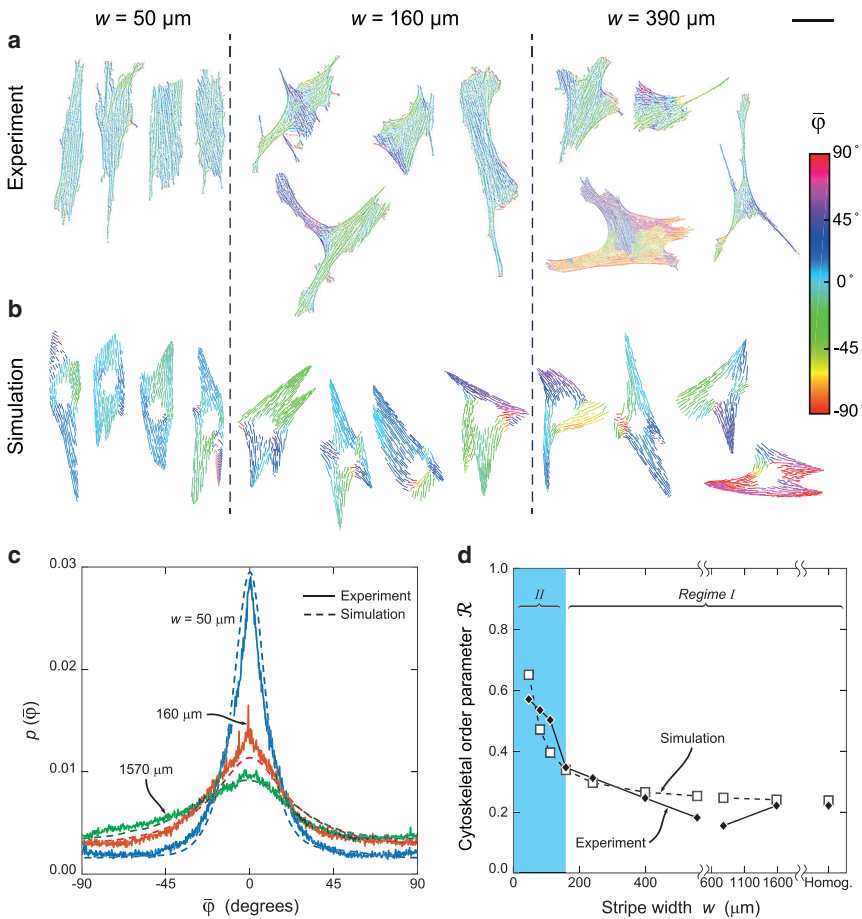
FIGURE 4 Experimental and computational data for the stress-fiber distributions. (*a*) Experiments and (*b*) simulations of the stress-fiber distributions within cells on three stripe widths *w* are shown. The region with no stress fibers is the passive nucleus in the 2D model. The stress fibers are colored by their orientation as parametrized by the measure $\overline{\varphi}$ that is invariant to rigid-body rotations of the cell. The scale bar in (*a*) and (*b*) represents 60 μm. (*c*) The corresponding predictions and measurements of the probability density functions $p(\overline{\varphi})$ over the ensemble of cell morphologies for three selected stripe widths are shown. (*d*) Predictions and measurements of the cytoskeletal order parameter $\mathcal{R}$ extracted from $p(\overline{\varphi})$ as a function of *w* are shown. The experimental data set in (*c*) and (*d*) comprised 50 observations, with both the experiments and simulations illustrating that cytoskeletal changes, as parametrized via stress-fiber polarization, only commence in regime II. To see this figure in color, go online.

framework, we shall now interrogate the model to better understand these regimes. In doing so, we shall now extract predictions from the model that are not easily measured but will aid our understanding of the underlying phenomena. However, we emphasize that these predictions use the precisely same model as used in the detailed comparisons with observations presented earlier with no further assumptions or approximations. The coarse-graining of the biochemical processes in the model results in the production of morphological entropy that is conjugated to a scalar parameter $1/\zeta$. By analogy with statistical thermodynamics, we call $1/\zeta$ homeostatic temperature. Thus, whereas $\mathcal{R}$ reflects the biochemical state of the cell as indicated by the experimentally measurable stress-fiber cytoskeleton, $1/\zeta$ is expected to capture the overall biochemical state of the cells. To illustrate this, we include predictions (Fig. 5 *a*) of the normalized homeostatic temperature $1/\widehat{\zeta}$ (see Supporting Materials and Methods, Section S2.5 for detailed definitions) as a function of stripe width. The homeostatic temperature $1/\widehat{\zeta}$ is invariant in regime I but rises sharply in regime II as cells undergo biochemical changes to maintain a homeostatic state when spatially constrained by narrow FN stripes. (We emphasize here that an increase in $1/\widehat{\zeta}$ with decreasing *w* in regime II does not imply a change in the average Gibbs free energy $\overline{G}$ of the cells in

the homeostatic ensemble because $\overline{G}$ is constrained to remain fixed at G_0 for all stripe widths; rather, an increase in $1/\widehat{\zeta}$ only quantifies the change of state of the cell in its attempt to maintain a homeostatic state.) Thus, similar to $\mathcal{R}$, the homeostatic temperature shows a clear delineation between the two regimes, and we shall use this understanding to employ other quantities suggested by the analogy with thermodynamics to more precisely define the regimes of contact guidance.

In classical thermodynamics, forces conjugated to the (internal) energy of a system are routinely defined as the force driving the system to reduce its energy (35–37). Similarly, entropic forces that originate from thermal fluctuations drive the system toward a state that maximizes its entropy and are thus conjugated to the entropy of the system (35–37). These force definitions unambiguously discriminate regimes in which the behavior of a system is governed either energetically or entropically. We shall use a similar strategy to more precisely characterize the two regimes of contact guidance. Recall that equilibrium of a system in contact with a thermal bath at temperature *T* is defined through the canonical ensemble with the thermodynamic driving force *F* given by $F \equiv \partial \mathcal{F} / \partial X_T$. Here, $\mathcal{F}$ is the Helmholtz potential, whereas *X* is the thermodynamic displacement conjugated to *F*. In an analogous
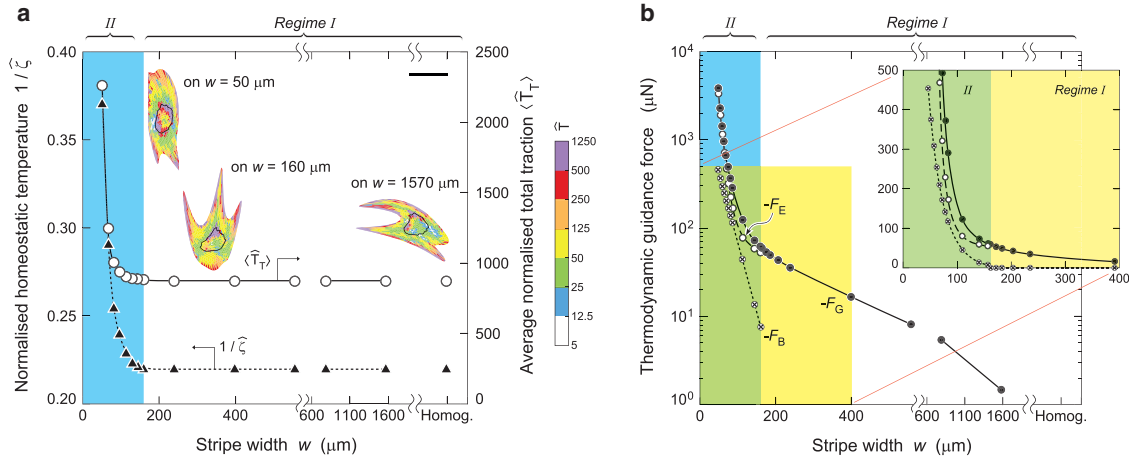
FIGURE 5 Homeostatic temperature, traction forces, and guidance forces. (*a*) Predictions of the variation of the normalized homeostatic temperature $1/\widehat{\zeta}$ and average normalized total traction force $\langle \widehat{T}_T \rangle$ with stripe width w. Predictions of the spatial distributions of normalized tractions $\widehat{T}$ are also included for randomly selected cell morphologies on three stripe widths (outline of nucleus shown as a black line) with the scale bars, 60 μm. Both homeostatic temperature and total traction forces only change with stripe width in regime II; see Supporting Materials and Methods, Section S2.5 for a more detailed discussion on the traction predictions. (*b*) Predictions of the total guidance force F_G as well as its entropic and biochemical components F_E and F_B, respectively, are shown as a function of w. The inset shows the variation using a linear scale for the forces and illustrates that $F_B = 0$ for $w > 160$ μm (regime I). To see this figure in color, go online.

manner, homeostatic statistical mechanics defines equilibrium of a living cell exchanging nutrients with its environment via the homeostatic ensemble, with the homeostatic potential $\mathcal{M}$ playing a role similar to the Helmholtz potential. The thermodynamic guidance force constraining the cells to lie within the FN stripes is then given by (see Supporting Materials and Methods, Section S3 for a more detailed definition and corresponding derivations)

$$F_G \equiv \left(\frac{\partial \mathcal{M}}{\partial w} \right)_\zeta. \tag{3}$$

Here, $\mathcal{M} \equiv \overline{G} - (1/\zeta)S_\Gamma$, with $\overline{G}$ the average Gibbs free energy of the cells in the homeostatic ensemble at homeostatic temperature $1/\zeta$, whereas S_Γ is the equilibrium morphological entropy of the cells. Thus, similar to classical thermodynamic forces, F_G comprises two components: 1) a biochemical contribution $F_B \equiv \partial \overline{G}/\partial w_\zeta$ resulting from the propensity of the cell to minimize the average Gibbs free energy of the morphological states it samples and 2) an entropic contribution $F_E \equiv -(1/\zeta)(\partial S_\Gamma/\partial w)_\zeta$ from the tendency of the cell to maximize its morphological entropy. Predictions of these forces as a function of stripe width (Fig. 5 *b*) illustrate that F_E is the dominant contributor to F_G over the full range of stripe widths, although $F_B \approx F_E$ for the narrowest stripes ($w = 50$ μm). Importantly, $F_B = 0$ for $w > 160$ μm (*inset* of Fig. 5 *b*), implying that only entropic forces contribute to the alignment of cells within these FN stripes. This unambiguously defines regime I as a purely entropic regime. Also, because both F_E and $F_B \neq 0$ in regime II ($w \leq 160$ μm), with their magnitudes being similar for the narrowest stripes, we refer to regime II as biochemically mediated.

Orientational alignment is a consequence of the tendency of cells to maximize morphological disorder

In regime I, the leading cell dimensions are smaller than the width of the FN stripes. Cells in this regime thus have the possibility to be completely orientationally disordered ($\Theta = 0$) but "choose" to orientationally order and align with the stripes. This alignment occurs because cells adhered near the stripe edges necessarily need to be aligned with the stripe direction. The question then remains as to why cells wander (migrate) toward the stripe edges, which in turn leads to an apparent decrease in their entropy (disorder). This behavior of individual cells is reminiscent of orientational ordering in a fluid of hard rods. In his study of a fluid of hard rods, Onsager (38) showed that although the orientational entropy of the ordered phase is lower than that of the isotropic phase, the total entropy of the orientationally ordered phase is higher than the isotropic (orientationally disordered) phase. This is because the orientationally ordered phase has a higher translational and hence total entropy because of the decrease of excluded volume caused by alignment. In other words, the system has traded off translational and orientational entropies so as to maximize its total entropy. We can extrapolate this idea to understand how the nonthermal fluctuations of individual cells result in them being orientationally ordered when seeded on the FN stripes.

To illustrate in a simplistic manner how this mechanism could be at play in our system, we examine a hard rod of length L in a channel of width w, with no part of the rod allowed to penetrate the channel edges (Similar to the FN
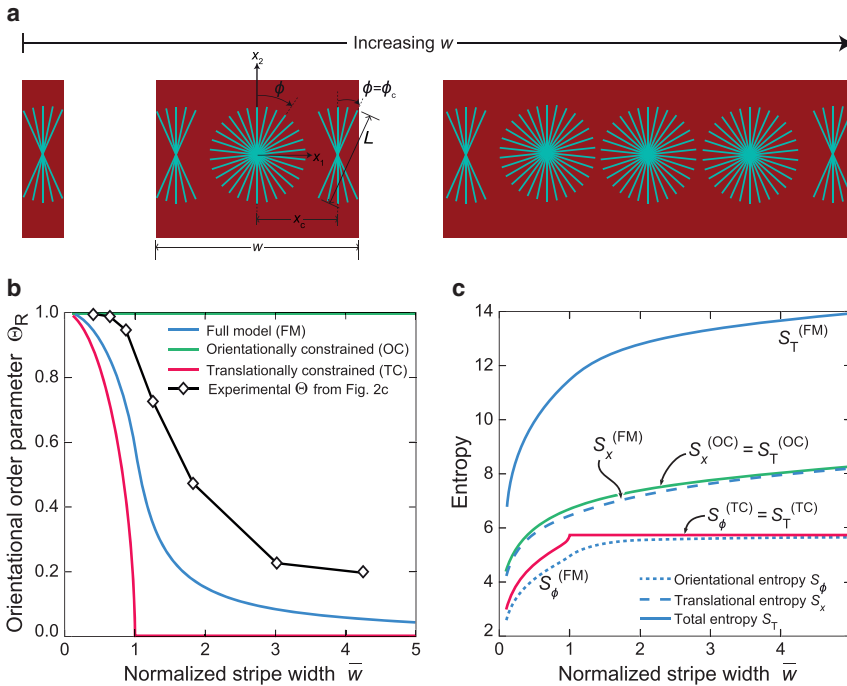
FIGURE 6 Entropic ordering of a hard rod of length L in a channel of width w. (a) A sketch illustrating the states the hard rod assumes as it translates and reorients within channels of three different normalized widths $\overline{w} \equiv w/L$ is given. Rod orientation is denoted by ϕ. (b) Predictions of the orientational order parameter Θ_R as a function of $\overline{w}$ are shown for the FM (*blue*) in which the rod has translational and orientational degrees of freedom, the TC model (*red*), and the OC model (*green*), compared with the cell-order parameter from experimental data on stripe widths normalized by the average cell length $2\ell_e$. (c) Corresponding predictions of the total entropy S_T, orientational entropy S_ϕ, and translational entropy S_X for the three models as a function of $\overline{w}$ are shown. The discrete entropies plotted here are for the choices of the total number of available orientational and translational states $N_\phi = 314$ and $1/\Delta\overline{w} = 800$, respectively (see Supporting Materials and Methods, Section S4 for definitions). To see this figure in color, go online.

stripes that restrict the cell by preventing cell adhesion outside the stripes, we use the terminology of "channel" to indicate that the walls of the channel restrict the motion of a hard rod. See Supporting Materials and Methods, Section S4 for further details). Three models are analyzed: 1) the full model (FM), in which the rod has both translational and rotational freedom; 2) the translationally constrained (TC) model, in which the rod centroid is pinned at the channel center $x_1 = 0$; and 3) the orientationally constrained (OC) model, in which the rod is constrained to be aligned with the channel ($\phi = 0$). Illustrations of the states the rod assumes in three channel sizes $\overline{w} \equiv w/L$ are included in Fig. 6 *a* for the FM. For the smallest channel size, the orientations of the rod are highly constrained because the rod is not able to explore an isotropic distribution of orientations ($-\pi/2 \leq \phi \leq \pi/2$). By contrast, for $\overline{w} \geq 1$, the rod assumes an isotropic distribution of orientations when located near the center of the channel, with the fraction of the channel width over which such isotropic distributions are possible increasing as $\overline{w}$ becomes larger. As a consequence, the orientational order parameter Θ_R of the rod (analogous to the orientational order parameter Θ of the cell) increases with decreasing $\overline{w}$ (Fig. 6 *b*), in a manner similar to that for cells on FN stripes (Fig. 2 *c*). By contrast, when the rod is TC, ordering occurs only for $\overline{w} < 1$ because the rod is unable to wander to the edges of the channel where it necessarily needs to align. Finally, when the rods are OC, $\Theta = 1$ for all $\overline{w}$.

To understand the preference of cells to follow a response consistent with the FM rather than a response in line with the TC model, we look at the corresponding entropies

(Fig. 6 *c*). We denote by $S_T^{(FM)}$ and $S_\phi^{(FM)}$ the total and orientational entropies, respectively, of the FM, whereas $S_T^{(TC)}$ is the total entropy of the TC model (and equal to its orientational entropy $S_\phi^{(TC)}$). Clearly, $S_T^{(TC)} > S_\phi^{(FM)}$ for all $\overline{w}$, but $S_T^{(FM)}$ is significantly higher than $S_T^{(TC)}$, i.e., the FM has gained a higher total entropy by trading off a small decrease in orientational entropy with a corresponding increase in its translational entropy. In other words, by allowing the rod to explore regions near the channel edges, one trades off a small decrease in orientational entropy with a larger increase in translational entropy, just as in the model of Onsager (36) for liquid crystals. Similarly, with $S_X^{(FM)}$ denoting the translational entropy of the FM and $S_T^{(OC)}$ the total entropy of the OC model (equal to its translational entropy $S_X^{(OC)}$), we observe that although $S_T^{(OC)} > S_X^{(FM)}$, $S_T^{(FM)}$ is significantly higher than $S_T^{(OC)}$.

In the experiments, fluctuations of the cell morphology are not orientationally or translationally restricted, with intracellular processes such as actin polymerization and treadmilling capable of equally changing cell shape or enabling rotation and translation of the cell. Thus, fluctuation of cell morphology will result in a maximization of morphological entropy, with the cell assuming states akin to that for the FM, as seen from the experimental cell-order parameter curve in Fig. 6 *b*. The maximization of morphological entropy results in partial ordering of specific observables, and here, cell alignment emerges from the drive of cells to maximize their overall state of disorder. This simple

hard rod model, although a powerful help to at least qualitatively understand orientational ordering in regime I, has significant limitations because it does not encode any information on the cell biochemistry. As a consequence, it not only fails to account for changes in cell morphology in regime II but also has quantitative limitations in predicting the cell-order parameter. The only parameter in the hard rod model is the rod length L, and it is natural to equate that to the length $2\ell_e = 130\ \mu m$ of the major axis of the cells. The measurements of Θ with the normalized stripe width interpreted as $\overline{w} \equiv w/(2\ell_e)$ are included in Fig. 6 *b*; clearly, although predictions of the hard rod model and the measurements have similar trends, the hard rod model significantly underpredicts the orientational ordering. The full homeostatic framework that includes critical biochemical processes such as the actomyosin stress-fiber remodelling (Fig. 1 *b*) are indeed essential not only to understand the regimes of contact guidance but also to make quantitative predictions of the wide range of observables reported here.

DISCUSSION

Contact guidance, the phenomenon by which cell alignment is influenced by anisotropic patterns, not only has implications for how cells organize themselves into collective entities such as tissues but is also critical in tissue engineering, in which the geometric structure of scaffolds can be used to control the morphology and organization of cells. Multiple hypotheses (8,17,18) have been proposed for rationalizing the sensing mechanisms that drive contact guidance. Although these theories highlight the role of specific cellular components, including filopodia, focal adhesion, or stress fibers, an understanding of why cells align with geometric or adhesive patterns has remained elusive.

Here, we use a statistical mechanics framework to interpret experimental data for the response of individual myofibroblasts on substrates with micropatterned stripes of FN and propose a, to our knowledge, novel explanation for contact guidance. This interpretation based on entropic considerations can be summarized as follows. The cell is an open system exchanging nutrients with its surrounding bath. Dynamic processes such as actin polymerization and treadmilling are driven by biochemical reactions fueled by these nutrients. These reactions are not precisely controlled, and thus fluctuations in the morphological states of the cell ensue, as widely recognized in the literature (39–41). These cell shape fluctuations occur on timescales longer than intracellular biochemical processes such as cytoskeletal remodelling and are ergodic in nature. This drives the cells toward a stationary state that is constrained by the fact that the coupled intracellular biochemical processes also strive to maintain the cell in a homeostatic state. These biochemical processes thus serve to provide both the mechanisms and

constraints for the maximization of morphological entropy, which is the principal ansatz of the model and does not require the explicit modeling of the dynamic processes, including the nutrient exchanges mentioned above. The entropy maximization assumptions allowed us to develop a statistical equilibrium formulation for the cell response and formalize the description of the nonthermal fluctuations through a homeostatic temperature $1/\zeta$ that is conjugated to the morphological entropy. Our simulations show that the normalized homeostatic temperature of the myofibroblasts is on the order of $1/\widehat{\zeta} \approx 0.2$ (Fig. 5 *a*), implying that $1/\zeta$ is typically $\sim 20\%$ of the average Gibbs free energy of all the morphological states the cell assumes. This translates to a homeostatic temperature $1/\zeta \approx 10^{12}$ K (Supporting Materials and Methods, Section S2), clearly illustrating the nonthermal nature of the cell shape fluctuations. These large Gibbs free-energy fluctuations allow cells to change shape, rotate, and wander over the FN stripes so as to maximize their morphological entropy. However, the spatial constraint of the FN stripes implies that cell morphologies close to the edges of the stripes need to be necessarily aligned with the edges of the stripes (Fig. 3). This results in an alignment of cells with the stripes that persists even when a representative cell size $2\ell_e \ll w$, and we refer to this as entropic contact guidance, labeled here as regime I. As the stripe width decreases to becomes of the order of $2\ell_e$, the spatial constraints imposed by the FN stripes induce biochemical changes within the cells that manifest as increases in the cell aspect ratio, greater polarization of the stress-fiber arrangements within the cell, and a significantly enhanced level of cell alignment. We refer to this as the biochemically mediated regime of contact guidance, labeled here as regime II.

The spatial constraint imposed by the FN stripes on cells imposes guidance forces F_G that constrain cells to lie within the stripes and align the cells with the stripe direction. These forces comprise two components: 1) an entropic component F_E associated with the drive of the cell to maximize its morphological entropy and 2) an energetic (or biochemical) component F_B resulting from the drive of the cell to reduce the average Gibbs free energy. It is thus natural to ask, what is the relation (if any) between the guidance force F_G and the traction forces exerted by cells on substrates? These traction forces are typically reported in experimental studies as measured via traction-force microscopy (42,43), although such measurements are difficult to perform on the glass substrates employed in this study. However, these tractions can be computed from our model, and predictions of normalized traction distributions $\widehat{T}(x_i)$ in randomly selected morphologies on three stripe widths are included in Fig. 5 *a* along with the variation of the average normalized total traction force $\langle \widehat{T}_T \rangle$ with w (see Supporting Materials and Methods, Section S2.5.1 for detailed definitions). The average total traction force $\langle \widehat{T}_T \rangle$ is invariant in regime I but rises in

regime II and clearly has a different functional dependence on stripe width compared with F_G shown in Fig. 5 *b*. We defer a detailed discussion of this issue of the differences between $\langle \widehat{T}_T \rangle$ and F_G to Supporting Materials and Methods, Section S3.2, but here it suffices to say that there is no direct relation between the forces exerted by cells on substrates via focal adhesions, which are of Newtonian nature, and the non-Newtonian guidance force F_G. Indeed, $F_G \rightarrow 0$ in the homogeneous substrate limit $w \rightarrow \infty$, although the traction forces exerted by cells on the substrate do not vanish in this limit. Nevertheless, it is intriguing to note here that the traction predictions suggest increasing tractions in regime II with decreasing *w*, even though both the measured and predicted cell areas remain relatively invariant. This is contrary to a common assumption, motivated by measurements on substrates of varying stiffness, that cell tractions scale with cell area. This scaling between tractions and cell area in response to mechanical cues seems to break down in response to the types of confinement cues investigated here. This is discussed more extensively in Supporting Materials and Methods, Section S2.5, but of course also requires future experimental validation.

Current models of active matter typically either use the notion of an effective temperature that is empirically defined (40) or resort to nonequilibrium approaches such as hydrodynamic theories for active gels, in which the concept of an affinity of energy carriers (e.g., ATP or GTP) is employed to maintain the system out of thermodynamic equilibrium (41). The statistical framework employed here combines the reductionist approach of the hydrodynamic active-matter theories with the simplicity of equilibrium formulations that employ an effective temperature. The key difference, however, lies in the fact that the homeostatic mechanics framework clearly defines the effective temperature within a statistical mechanics context, along with its conjugated entropy. The overall homeostatic mechanics framework is independent of the biochemical model used to describe the intracellular processes and the free energy of a specific morphological microstate. Here, to model contact guidance, we only considered contributions from the remodelling of the actomyosin cytoskeleton and the passive elasticity of the cytoplasm as well as the nucleus, along with adhesions that equilibrate forces generated by these cellular components (Fig. 1 *b*). Thus, the kinetics of signaling pathways such as Rho signaling cascade triggered by the formation of focal adhesions and resulting in the polymerization of stress fibers are not explicitly modeled. Rather, in this equilibrium framework, the cytoskeletal structures and focal adhesion distributions as well as cell morphologies emerge as interlinked coupled phenomena. In fact, contact guidance is a direct outcome of the fact that near the stripe edges, the focal adhesion and cytoskeletal structures are restricted by the FN patterns, and this in turn imposes restrictions on the morphologies that are accessible over the course of the nonthermal fluctuations that the cells undergo.

In summary, we have shown that contact guidance of myofibroblasts by FN stripes can be understood in terms of classical concepts of statistical thermodynamics, namely, entropy maximization subject to appropriate constraints. To make these concepts applicable to the context of nonthermal morphological fluctuations of cells, we had to employ nonclassical notions of entropy borrowed from information theory. This framework shows convincingly that contact guidance is based on physical forces of thermodynamic origin because of shape fluctuations of the cell. The impact of this is multifold:

1) Because the fluctuations are of biochemical rather than of thermal origin, we do not need to invoke unrealistic thermal fluctuation energies to rationalize the behavior of cells. The homeostatic mechanics framework formalizes this notion of an effective temperature of cells by recognizing that the fluctuations are related to the energy fluctuations resulting from nutrient exchanges with the nutrient bath.

2) Our model predicts, with remarkable fidelity, not only trends but also the statistical variability of a wide range of biological observables using a single set of parameters to describe the cell. Indeed, the mechanism of contact guidance we propose here, viz., that contact guidance (or orientational ordering) emerges from the drive of cells to maximize the disorder of the morphological states they assume is inherently linked to this statistical variability.

3) The concept of maximization of morphological entropy subject to the constraint of homeostasis is very general and can be used to predict guidance as a function of cell phenotype as well as a range of biophysical and/or biochemical cues. For example, in Supporting Materials and Methods, Section S2.6, we explore the question of whether the reduced stiffness of cancer cells (44) may result in enhanced contact guidance, thereby promoting tissue invasion via contact guidance (45,46). However, it remains to be seen via both experiments and corresponding predictions how widely the ansatz of maximization of morphological entropy constrained by homeostasis is applicable to rationalize the response of different cell phenotypes to environmental cues more general than the ones examined in this study.

SUPPORTING MATERIAL

AUTHOR CONTRIBUTIONS

the numerical data, and created the figures. S.S.S., A.V., and H.S. contributed in developing the numerical codes for the model. C.V.C.B., N.A.K., A.D., and V.S.D. designed and supervised the project. V.S.D. wrote the manuscript, aided by many insightful discussions with A.D. All authors provided critical comments and edited the manuscript.

ACKNOWLEDGMENTS

SUPPORTING CITATIONS

References (47–65) appear in the Supporting Material.

REFERENCES

1. Chien, K. R., I. J. Domian, and K. K. Parker. 2008. Cardiogenesis and the complex biology of regenerative cardiovascular medicine. *Science.* 322:1494–1497.

2. Smith, L., Y. Xia, …, S. Thomopoulos. 2012. Tissue-engineering strategies for the tendon/ligament-to-bone insertion. *Connect. Tissue Res.* 53:95–105.

3. Provenzano, P. P., and R. Vanderby, Jr. 2006. Collagen fibril morphology and organization: implications for force transmission in ligament and tendon. *Matrix Biol.* 25:71–84.

4. Doyle, A. D., F. W. Wang, …, K. M. Yamada. 2009. One-dimensional topography underlies three-dimensional fibrillar cell migration. *J. Cell Biol.* 184:481–490.

5. Ramirez-San Juan, G. R., P. W. Oakes, and M. L. Gardel. 2017. Contact guidance requires spatial control of leading-edge protrusion. *Mol. Biol. Cell.* 28:1043–1053.

6. Weiss, P. 1945. Experiments on cell and axon orientation in vitro; the role of colloidal exudates in tissue organization. *J. Exp. Zool.* 100:353–386.

7. Tamiello, C., A. B. C. Buskermolen, …, C. V. C. Bouten. 2016. Heading in the right direction: understanding cellular orientation responses to complex biophysical environments. *Cell. Mol. Bioeng.* 9:12–37.

8. Dunn, G. A., and J. P. Heath. 1976. A new hypothesis of contact guidance in tissue cells. *Exp. Cell Res.* 101:1–14.

9. Meyle, J., K. Gültig, …, W. Nisch. 1994. Contact guidance of fibroblasts on biomaterial surfaces. *J. Mater. Sci. Mater. Med.* 5:463–466.

10. den Braber, E. T., J. E. de Ruijter, …, J. A. Jansen. 1996. Quantitative analysis of fibroblast morphology on microgrooved surfaces with various groove and ridge dimensions. *Biomaterials.* 17:2037–2044.

11. Chua, J. S., C. P. Chng, …, E. K. Yim. 2014. Extending neurites sense the depth of the underlying topography during neuronal differentiation and contact guidance. *Biomaterials.* 35:7750–7761.

12. Ray, A., O. Lee, …, P. P. Provenzano. 2017. Anisotropic forces from spatially constrained focal adhesions mediate contact guidance directed cell migration. *Nat. Commun.* 8:14923.

13. Provenzano, P. P., D. R. Inman, …, P. J. Keely. 2008. Contact guidance mediated three-dimensional cell migration is regulated by Rho/ROCK-dependent matrix reorganization. *Biophys. J.* 95:5374–5384.

14. Wang, J., J. W. Petefish, …, I. C. Schneider. 2015. Epitaxially grown collagen fibrils reveal diversity in contact guidance behavior among cancer cells. *Langmuir.* 31:307–314.

15. Barthes, J., H. Özçelik, …, N. E. Vrana. 2014. Cell microenvironment engineering and monitoring for tissue engineering and regenerative medicine: the recent advances. *BioMed Res. Int.* 2014:921905.

16. Gasiorowski, J. Z., C. J. Murphy, and P. F. Nealey. 2013. Biophysical cues and cell behavior: the big impact of little things. *Annu. Rev. Biomed. Eng.* 15:155–176.

17. Ohara, P. T., and R. C. Buck. 1979. Contact guidance in vitro. A light, transmission, and scanning electron microscopic study. *Exp. Cell Res.* 121:235–249.

18. Curtis, A. S. G., and P. Clark. 1990. The effects of topographic and mechanical properties of materials on cell behavior. *CRC Rev. Biocompatibility.* 5:343–362.

19. Théry, M. 2010. Micropatterning as a tool to decipher cell morphogenesis and functions. *J. Cell Sci.* 123:4201–4213.

20. D'Arcangelo, E., and A. P. McGuigan. 2015. Micropatterning strategies to engineer controlled cell and tissue architecture in vitro. *Biotechniques.* 58:13–23.

21. Duclos, G., S. Garcia, …, P. Silberzan. 2014. Perfect nematic order in confined monolayers of spindle-shaped cells. *Soft Matter.* 10:2346–2353.

22. Reinhart-King, C. A., M. Dembo, and D. A. Hammer. 2008. Cell-cell mechanical communication through compliant substrates. *Biophys. J.* 95:6044–6051.

23. Yang, M. T., J. Fu, …, C. S. Chen. 2011. Assaying stem cell mechanobiology on microfabricated elastomeric substrates with geometrically modulated rigidity. *Nat. Protoc.* 6:187–213.

24. Buskermolen, A. B. C., N. A. Kurniawan, and C. V. C. Bouten. 2018. An automated quantitative analysis of cell, nucleus and focal adhesion morphology. *PLoS One.* 13:e0195201.

25. Shishvan, S. S., A. Vigliotti, and V. S. Deshpande. 2018. The homeostatic ensemble for cells. *Biomech. Model. Mechanobiol.* 17:1631–1662.

26. Recordati, G., and T. G. Bellini. 2004. A definition of internal constancy and homeostasis in the context of non-equilibrium thermodynamics. *Exp. Physiol.* 89:27–38.

27. Weiss, T. F. 1996. Cellular Biophysics. MIT Press, Cambridge, MA.

28. Shenoy, V. B., H. Wang, and X. Wang. 2016. A chemo-mechanical free-energy-based approach to model durotaxis and extracellular stiffness-dependent contraction and polarization of cells. *Interface Focus.* 6:20150067.

29. Vigliotti, A., R. M. McMeeking, and V. S. Deshpande. 2015. Simulation of the cytoskeletal response of cells on grooved or patterned substrates. *J. R. Soc. Interface.* 12:20141320.

30. Vigliotti, A., W. Ronan, …, V. S. Deshpande. 2016. A thermodynamically motivated model for stress-fiber reorganization. *Biomech. Model. Mechanobiol.* 15:761–789.

31. Suresh, H., S. S. Shishvan, and A. Vigliotti. 2019. Homeostatic ensemble of cells on stripes (Version v2.0). Zenodo. http://doi.org/10.5281/zenodo.2576540.

32. Mamaghani, P., and A. M. Donald. 2018. The impact of fibronectin stripe patterns on the cellular and nuclear morphology of fibroblasts. *bioRxiv* https://doi.org/10.1101/302687.

33. Zemel, A., F. Rehfeldt, …, S. A. Safran. 2010. Optimal matrix rigidity for stress fiber polarization in stem cells. *Nat. Phys.* 6:468–473.

34. Gupta, M., B. R. Sarangi, …, B. Ladoux. 2015. Adaptive rheology and ordering of cell cytoskeleton govern matrix rigidity sensing. *Nat. Commun.* 6:7525.

35. Reif, F. 2009. Fundamentals of Statistical and Thermal Physics. Waveland Press, Long Grove, IL.

36. Dill, K. A., and S. Bromberg. 2003. Molecular Driving Forces: Statistical Thermodynamics in Chemistry and Biology. Garland Science, New York.

37. Kuzemsky, A. L. 2017. Statistical Mechanics and the Physics of Many-Particle Model Systems. World Scientific, Singapore.

38. Onsager, L. 1949. The effects of shape on the interaction of colloidal particles. *Ann. N. Y. Acad. Sci.* 51:627–659.

39. Brangwynne, C. P., F. C. MacKintosh, and D. A. Weitz. 2007. Force fluctuations and polymerization dynamics of intracellular microtubules. *Proc. Natl. Acad. Sci. USA.* 104:16128–16133.

40. Gov, N. S., and S. A. Safran. 2005. Red blood cell membrane fluctuations and shape controlled by ATP-induced cytoskeletal defects. *Biophys. J.* 88:1859–1874.

41. Joanny, J. F., and J. Prost. 2009. Active gels as a description of the actin-myosin cytoskeleton. *HFSP J.* 3:94–104.

42. Chang, S. S., W. H. Guo, …, Y. L. Wang. 2013. Guidance of cell migration by substrate dimension. *Biophys. J.* 104:313–321.

43. Franck, C., S. Hong, …, G. Ravichandran. 2007. Three-dimensional full-field measurements of large deformations in soft materials using confocal microscopy and digital volume correlation. *Exp. Mech.* 47:427–438.

44. Hayashi, K., and M. Iwata. 2015. Stiffness of cancer cells measured with an AFM indentation method. *J. Mech. Behav. Biomed. Mater.* 49:105–111.

45. Hartmann, N., N. A. Giese, …, E. Ryschich. 2014. Prevailing role of contact guidance in intrastromal T-cell trapping in human pancreatic cancer. *Clin. Cancer Res.* 20:3422–3433.

46. Wang, J., and I. C. Schneider. 2017. Myosin phosphorylation on stress fibers predicts contact guidance behavior across diverse breast cancer cells. *Biomaterials.* 120:81–93.

47. Haralick, R. M., and L. G. Shapiro. 1992. Computer and Robot Vision. Addison-Wesley, Boston, MA.

48. Obbink-Huizer, C., J. Foolen, …, F. P. Baaijens. 2014. Computational and experimental investigation of local stress fiber orientation in uniaxially and biaxially constrained microtissues. *Biomech. Model. Mechanobiol.* 13:1053–1063.

49. Frangi, A. F., W. J. Niessen, …, M. A. Viergever. 1998. Multiscale vessel enhancement filtering. *In* Medical Image Computing and Computer-Assisted Intervention — MICCAI, Lecture Notes in Computer Science. W. M. Wells, A. Colchester, and S. Delp, eds. Springer.

50. Jaynes, E. T. 1957. Information theory and statistical mechanics. *Phys. Rev.* 106:620–630.

51. Deshpande, V. S., R. M. McMeeking, and A. G. Evans. 2006. A bio-chemo-mechanical model for cell contractility. *Proc. Natl. Acad. Sci. USA.* 103:14015–14020.

52. He, S., Y. Su, …, H. Gao. 2014. Some basic questions on mechanosensing in cell-substrate interaction. *J. Mech. Phys. Solids.* 70:116–135.

53. Sanz-Herrera, J. A., P. Moreo, …, M. Doblaré. 2009. On the effect of substrate curvature on cell mechanics. *Biomaterials.* 30:6674–6686.

54. Ogden, R. W. 1972. Large deformation isotropic elasticity – on the correlation of theory and experiment for incompressible rubberlike solids. *Proc. R. Soc. Lond. A Math. Phys. Sci.* 326:565–584.

55. Metropolis, N., A. W. Rosenbluth, …, E. Teller. 1953. Equation of state calculations by fast computing machines. *J. Chem. Phys.* 21:1087–1092.

56. Lucas, S. M., R. L. Ruff, and M. D. Binder. 1987. Specific tension measurements in single soleus and medial gastrocnemius muscle fibers of the cat. *Exp. Neurol.* 95:142–154.

57. Tan, J. L., J. Tien, …, C. S. Chen. 2003. Cells lying on a bed of microneedles: an approach to isolate mechanical force. *Proc. Natl. Acad. Sci. USA.* 100:1484–1489.

58. Maskarinec, S. A., C. Franck, …, G. Ravichandran. 2009. Quantifying cellular traction forces in three dimensions. *Proc. Natl. Acad. Sci. USA.* 106:22108–22113.

59. Califano, J. P., and C. A. Reinhart-King. 2010. Substrate stiffness and cell area predict cellular traction stresses in single cells and cells in contact. *Cell. Mol. Bioeng.* 3:68–75.

60. Oakes, P. W., S. Banerjee, …, M. L. Gardel. 2014. Geometry regulates traction stresses in adherent cells. *Biophys. J.* 107:825–833.

61. Rape, A. D., W. H. Guo, and Y. L. Wang. 2011. The regulation of traction force in relation to cell shape and focal adhesions. *Biomaterials.* 32:2043–2051.

62. Prager-Khoutorsky, M., A. Lichtenstein, …, A. D. Bershadsky. 2011. Fibroblast polarization is a matrix-rigidity-dependent process controlled by focal adhesion mechanosensing. *Nat. Cell Biol.* 13:1457–1465.

63. Dumbauld, D. W., T. T. Lee, …, A. J. García. 2013. How vinculin regulates force transmission. *Proc. Natl. Acad. Sci. USA.* 110:9788–9793.

64. Kenney, J. F., and E. S. Keeping. 1951. Mathematics of Statistics, Pt. 2, Second Edition. Van Nostrand, Princeton, NJ.

65. Westfall, P. H. 2014. Kurtosis as peakedness, 1905 - 2014. R.I.P. *Am. Stat.* 68:191–195.